Dynamic warming of deep Atlantic water masses during the last deglaciation

Jiaxu Zhang[1]*, Zhengyu Liu[1]*, Esther C. Brady[2], Alexandra Jahn[3], Delia W. Oppo[4], Peter U. Clark[5], Shaun A. Marcott[6] & Keith Lindsay[2]

[1]Department of Atmospheric and Oceanic Sciences and Center for Climatic Research, University of Wisconsin-Madison, Madison, Wisconsin 53706, USA.

[2]Climate and Global Dynamics Division, National Center for Atmospheric Research, Boulder, Colorado 80307, USA.

[3]Department of Atmospheric and Oceanic Sciences and the Institute of Arctic and Alpine Research, University of Colorado Boulder, Boulder, Colorado 80309, USA.

[4]Department of Geology and Geophysics, Woods Hole Oceanographic Institution, Woods Hole, Massachusetts 02543, USA.

[5]Department of Geosciences, Oregon State University, Corvallis, Oregon 97331, USA.

[6]Department of Geoscience, University of Wisconsin-Madison, Madison, Wisconsin 53706, USA.

*e-mail: jzhang76@wisc.edu, zliu3@wisc.edu

Changes in the Atlantic deep-ocean water masses during the last deglaciation played a critical role in regulating changes in global climate and the carbon cycle[1,2]. The $\delta^{18}O$ of benthic foraminiferal calcite ($\delta^{18}O_c$) is commonly used as a tracer to infer changes in Atlantic water masses associated with a reduced AMOC[3,4], with high-resolution deep-sea records revealing a lead of North Atlantic $\delta^{18}O_c$ over that of the Southern Ocean early during the last deglaciation[5]. However, interpretation of this phasing and its implication for the carbon cycle remains controversial[5–9] because of the unknown combination of water temperature and oxygen isotopic composition of the water ($\delta^{18}O_w$) to the $\delta^{18}O_c$ signals. Here we use an isotope-enabled ocean general circulation model under realistic transient climate forcing to provide a dynamic framework for understanding deglacial $\delta^{18}O_c$ signals. Model results suggest that input from both northern and southern sources into the ocean interior decreased in response to North Atlantic freshwater forcing, and the deep North Atlantic warmed by 1.4°C due to enhanced diapycnal mixing. This dynamic warming, rather than changes in the relative contribution of water mass sources as previously assumed, is the main cause of the observed $\delta^{18}O_c$ phase differences.

Changes in the deglacial Atlantic deep-ocean water masses were particularly pronounced during Heinrich Stadial 1 (HS1; 17.5–14.7 ka), when a significantly reduced AMOC[10] led to a strong cooling in the Northern Hemisphere coupled with a warming in the Southern Hemisphere, possibly contributing to the early deglacial rise of the atmospheric CO_2[11,12]. However, the behavior of the deep Atlantic water masses is poorly constrained during HS1, which limits our understanding of how CO_2 that accumulated in the deep ocean during the last glacial period was released to the atmosphere[2,13]. Based on the phase difference of high-resolution deep-sea benthic $\delta^{18}O_c$ records between the North Atlantic and the Southern Ocean during HS1[5], some studies suggest that it reflects northward expansion of southern-sourced deep water[6,7], whereas others conclude that northern-sourced waters continued to fill much of the intermediate and deep Atlantic despite a reduced AMOC[5,8,9]. To better constrain the deglacial water-mass behavior, attention has to be turned either to development of high-resolution temperature (e.g. Mg/Ca) reconstructions, which has proven to be difficult for deep-ocean cores[14], or to numerical models as an independent line of evidence, which is the focus of this study.

A challenge faced by numerical models in understanding the deglacial evolution of the deep ocean is that most simulation results cannot be compared directly against proxy records of circulation changes, either because the models do not simulate the same variables estimated by proxies[15–17] or because the climate forcing and experimental setup are too idealized[15,18–20]. Here, we address this challenge by performing the first deglacial ocean circulation-$\delta^{18}O_w$ coevolving transient simulation in a state-of-the-art isotope-enabled ocean general circulation model [Parallel Ocean Program version 2 (iPOP2)] (Methods). This simulation were conducted from the Last Glacial Maximum (LGM) at 22 ka to the late Bølling-Allerød Interstadial (B-A) at 13 ka, and forced by climate variables from a realistic transient simulation of the last deglaciation in a fully coupled climate model (TRACE21) (Supplementary Fig. 1) which successfully reproduced many observed features of the deglacial climate[12,16,21,22]. Our ocean modeling also quantifies the contribution of local water temperature to $\delta^{18}O_c$ (~0.25‰ °C^{-1}; ref. 23) (Methods), thus providing a dynamic framework for understanding the mechanisms responsible for the evolution of $\delta^{18}O_c$ during the last deglaciation.

Our modeling shows that during the LGM, Antarctic Bottom Water (AABW) formed due to brine rejection associated with sea-ice expansion around Antarctica that, along with a vigorous counterclockwise abyssal overturning[24] (Supplementary Fig. 2c and d), caused the AABW to fill the entire deep Atlantic[25]. During HS1, freshwater forcing nearly shut down North Atlantic Deep Water (NADW) formation (from 15 Sv to 2.5 Sv), while a lesser decrease (from 6.5 Sv to 5 Sv) in AABW formation occurred due to surface warming and reduced brine rejection (Supplementary Fig. 1; 2e and f). This decrease in ventilation of the deep North Atlantic (NA) by northern and southern sources resulted in it becoming isolated, with only slow renewal by AABW through the abyssal overturning. These simulated changes in ocean circulation are consistent with the Pa/Th ratio at Bermuda[10] as a proxy for the AMOC intensity (Fig. 1b) and the radiocarbon benthic-planktonic age offset at Iberian Margin[26] as a proxy for the apparent ventilation ages (Fig. 1c, Methods). Moreover, the simulated ocean circulation successfully reproduces the basin-wide pattern and amplitude of the observed $\delta^{18}O_c$ changes across the Atlantic between the LGM and late HS1 [Fig. 2, pattern correlation r = 0.87 (Supplementary Fig. 3)]. In particular, the model and data are characterized by greatest changes in the upper NA and little change in the deep Southern Ocean (SO). Meanwhile, many other features of the modeled $\delta^{18}O_c$ agree with observations (Supplementary Fig. 4, 5 and 10).

To examine the regional phasing of the deep $\delta^{18}O_c$ response, we compared our simulation results with two well-dated, high-resolution benthic $\delta^{18}O_c$ records, one from the Iberian Margin in the NA (MD99-2334K, 37.8°N, 3146 m)[6,27] and the other in the Atlantic sector of the SO (MD07-3076Q, 44.2°S, 3770 m)[5]. These cores also have bottom-water temperature reconstructions, allowing us to evaluate whether the reasons for the $\delta^{18}O_c$ changes in the model are the same as those inferred for the observations. In both the model and the records (Fig. 1d), $\delta^{18}O_c$ shows a gradual post-glacial increase from 22 ka to 19 ka, which is due to a lagged response of the deep ocean to the maximum enrichment of $\delta^{18}O_w$ in the upper ocean during the LGM (Methods). From

19 ka to late HS1 (16 ka), the modeled $\delta^{18}O_c$ trend reverses and captures the observed earlier and greater $\delta^{18}O_c$ decrease in the NA (~0.6‰) than in the SO (~0.2‰)[5] (Fig. 1d).

The cause of this earlier $\delta^{18}O_c$ decrease at deep NA core sites during HS1 is widely debated. One "southern-source" hypothesis suggests that reduced formation of NADW during HS1 enhanced the formation and northward expansion of southern-sourced low-$\delta^{18}O$, low-$\delta^{13}C$ AABW[6,7]. An alternative "northern-source" hypothesis argues that during HS1, the NA was influenced by overflows of brine-generated deep water formed by sea-ice expansion in the Nordic Seas, with the low $\delta^{18}O$ signal reflecting meltwater transferred to depth during brine formation[5,8,9] and the low $\delta^{13}C$ values reflecting suppressed air-sea gas exchange[5]. Temperature may also have played a role in affecting the deglacial $\delta^{18}O_c$ signal, but the sign, magnitude, and mechanisms of temperature change are highly uncertain[3,6,7,22].

In this context, our model results indicate that the apparent lead of the deglacial $\delta^{18}O_c$ decrease in the deep NA over the SO is due to earlier warming in the north rather than to a change in southern- or northern-sourced water masses. During HS1, the simulated $\delta^{18}O_w$ component shows nearly coherent decreases at both core sites (Fig. 1e). These depletions at depth are caused primarily by the transfer of ^{18}O-depleted surface meltwater, with a change of the surface precipitation and evaporation also playing a small role (Methods, Supplementary Fig. 8). Although the decrease of NA $\delta^{18}O_w$ is slightly greater since the site is closer to the meltwater source, the difference is nearly indistinguishable and cannot explain the much larger differences seen in the records. In contrast, the temperature component exhibits strong asynchrony, with the deep ocean below 3000 m warming by ~1.4°C in the north but experiencing little change in the south, consistent with Mg/Ca temperature reconstructions from the cores[6,13] (Fig. 1f). The warming in the north causes $\delta^{18}O_c$ to decrease by 0.35‰, thus explaining most of the 0.4‰ difference between the two records.

The relative contributions of $\delta^{18}O_w$ and temperature can be seen more clearly in the basin-wide responses (Fig. 3). In response to the input of ^{18}O-depleted freshwater during HS1, $\delta^{18}O_w$ and salinity decrease over the entire basin relative to their LGM values (Fig. 3e and Supplementary Fig. 7g). A considerable portion of the ^{18}O-depleted freshwater is trapped in the upper NA and within the Labrador Sea and the Nordic Seas due to the strong reduction in deep-water formation and associated overflows (Supplementary Fig. 2d and f). If the AMOC did not weaken, this extra ^{18}O would be transported into the ocean interior (Methods, Supplementary Fig. 9). A modest anomaly tongue (~−0.1‰) extends downward and southward along the lower limb of the diminishing glacial AMOC during the transition to HS1, and further disperses into the whole ocean through the remaining circulation and general mixing (Fig. 3e). In contrast, the temperature response shows a bipolar seesaw response at the surface and basin-wide warming in the subsurface[16,22] (Fig. 3f). Notably, the warming occurs all the way to the abyss in the NA but not in the SO, consistent with observations[6,13,28], generating a deep meridional temperature gradient that accounts for the $\delta^{18}O_c$ gradient across the deep Atlantic.

We identify different physical processes as responsible for the different $\delta^{18}O_w$ and temperature responses during HS1 (Fig. 4 and Methods). During the LGM, $\delta^{18}O_w$ is increasingly depleted with depth (Fig. 3a), and the $\delta^{18}O_w$ tracer budget at 3100 m in the NA is dominated by the horizontal mean advection (Supplementary Fig. 11b). During HS1, this vertical gradient reverses in the NA, due to the highly ^{18}O-depleted freshwater input trapped near the surface. This reversed gradient weakens with depth (Fig. 3c) because neither mean advection nor diapycnal mixing can effectively bring the surface signal down to depth in the absence of deep convection

(Fig. 4a and Supplementary Fig. 11). The deep NA therefore experiences little $\delta^{18}O_w$ change (Fig. 3e) even though it is geographically closer to the freshwater input.

In contrast to the passive response of $\delta^{18}O_w$, the temperature response involves dynamic processes that can cause warming or cooling at depth (Fig. 4b). During the LGM, the heat budget of the deep NA is also dominated by horizontal mean advection (Supplementary Fig. 12b). During HS1, the collapse of the AMOC reduces the horizontal advection by more than 90%. This reduced AMOC has traditionally been speculated to cause a deep warming by reducing the vertical advection (i.e., the cold-water upwelling)[29]. However, the heat budget shows that the deep warming is caused by an enhanced downward heat flux associated with diapycnal mixing that overwhelms an enhanced cold upwelling advection (Supplementary Fig. 12b). The unexpected increase of vertical advection is caused by a marked increase of vertical temperature gradient ($\partial T/\partial z$) rather than the upwelling velocity (Supplementary Fig. 13). During HS1, the cessation of deep convection in the subpolar NA prevents transmission of intense atmospheric cooling to the subsurface ocean, generating a strong mid-depth warming due to heat accumulation[22,30], and, in turn, an increased $\partial T/\partial z$ below. Both the diapycnal mixing and vertical advection are actually enhanced by this increased $\partial T/\partial z$. It is therefore the enhanced diapycnal mixing induced by the strong mid-depth warming that effectively heats the deep NA. In contrast, the SO temperatures increase in the upper layers due to reduced northward oceanic heat transport, but change little at depth. Close to the deep SO mean temperature front (~40°S), the heat budget is balanced between a cold eddy heat transport (a major component in horizontal mixing) and a warm tendency of other processes (Supplementary Fig. 12c). Reduced AABW formation and associated mass transport in the abyssal overturning decreases the northward advection of cold AABW, tending to induce warming at depth. However, this warming tendency is largely offset by the enhanced cooling from eddy transport, so that SO warming is confined to the upper ocean (Fig. 3f).

Our study highlights the role of deep warming in the deglacial evolution of deep water masses and illustrates a new mechanism for this warming. Moreover, our strategy of direct and quantitative model-proxy comparison provides a new perspective to understand the mechanism of many deglacial benthic $\delta^{18}O_c$ records (see Methods for other examples), and ultimately the cause of the evolution of the deep-ocean circulation, global climate, and the carbon cycle.

Acknowledgements This work is supported by the U.S. NSF P2C2 projects (1401778 and 1401802), DOE DE-SC0006744, the Wisconsin Alumni Research Foundation, China NSFC 41130105, and Chinese MOST 2012CB955201. We thank B. Otto-Bliesner for her support throughout the work; J. Gottschalk, J. Zhu, and A. Hu for helpful discussions; G. Danabasoglu, D. Bailey, and S. Bates for modeling technical assistance; and J. Roberts, D. Lund, and L. Skinner for providing data. The simulation was conducted at the National Center for Atmospheric Research supercomputing facility.

Author Contributions J.Z. and Z.L. designed the study. J.Z., E.B., A.J., and K.L. developed the isotope tracer modules of the ocean model. J.Z. performed the deglacial transient simulation and analyzed the model output. D.O., P.C., and S.M. helped with the model-data comparison. J.Z., Z.L., and P.C. wrote the paper. All authors discussed the results and commented on the manuscript.

Additional Information Supplementary information is available in the online version of the paper. Reprints Reprints and permissions information is available at www.nature.com/reprints. Correspondence and requests for materials should be addressed to J.Z. and Z.L.

Competing financial interests

The authors declare no competing financial interests.

Figure legends

Figure 1 | Model deglacial signals compare with proxies. a, Atmospheric CO_2 concentration (orange) and freshwater fluxes of the Northern (navy) and Southern (blue) Hemispheres applied in TRACE21[16]. **b**, Pa/Th ratio at Bermuda (GGC5[10]) as a proxy for the strength of AMOC and model maximum AMOC transport (below 500 m). **c**, ^{14}C benthic-planktonic (B-P) age offset at Iberian Margin (MD99-2334K[26]) and model abiotic ^{14}C B-P age[31] at this site. **d**, Benthic $\delta^{18}O_c$ at Iberian Margin (MD99-2334K[6,27], green) and Southern Ocean (MD07-3076Q[5], pink), and model $\delta^{18}O_c$ at the corresponding sites. **e**, Model water isotopic concentration $\delta^{18}O_w$ at the two core sites described in (**d**). Reconstructed $\delta^{18}O_w$ of MD99-2334K[6] and MD07-3076Q[13] are offset by +0.3‰ and −0.5‰, respectively. Global mean $\delta^{18}O_w$ (gray) is converted from ice-volume equivalent sea level[32] by 1.05‰/145 m. **f**, Same as (**e**), but for water temperatures. Mg/Ca temperature of MD07-3076Q[13] is offset by −3°C. All dashed lines indicate proxies, and solid lines indicate model results. HS1, Heinrich Stadial 1; B-A, Bølling-Allerød; YD, Younger Dryas.

Figure 2 | Deglacial benthic $\delta^{18}O_c$ changes in the Atlantic. Contours are zonally averaged Atlantic $\delta^{18}O_c$ changes between late HS1 (16-15 ka mean) and glacial (20-19 ka mean) in the model. Circles and squares are reconstructed benthic $\delta^{18}O_c$ changes (Supplementary Table 1) between these two periods. Squares indicate the two cores sites of Fig. 1d.

Figure 3 | Atlantic zonally averaged $\delta^{18}O_w$ (left column) and temperature (right column). From top to bottom panels are variables at 19 ka (**a-b**), 16 ka (**c-d**), and their differences (**e-f**).

Squares indicate the two core sites of Fig. 1d. The deep North Atlantic core site experiences reversed $\delta^{18}O_w$ vertical gradient and enlarged temperature vertical gradient from 19 ka to 16 ka.

Figure 4 | Schematic of the passive $\delta^{18}O_w$ tracer response (a) and dynamic temperature response (b) during HS1. The cessation of deep convection confines the light, ^{18}O-depleted freshwater input at upper layers in the NA, but accumulates heat at intermediate depth, which enlarges the temperature gradient below and enhances the downward heat flux by diapycnal mixing. The deep NA therefore experiences little $\delta^{18}O_w$ change but a significant warming of ~1.4°C. In the deep SO, reduced AABW decreases the cold water transport, tending to cause warming. But the enhanced cooling from eddy advection near the mean temperature front cancels most of this tendency and retains the temperature.

Figures

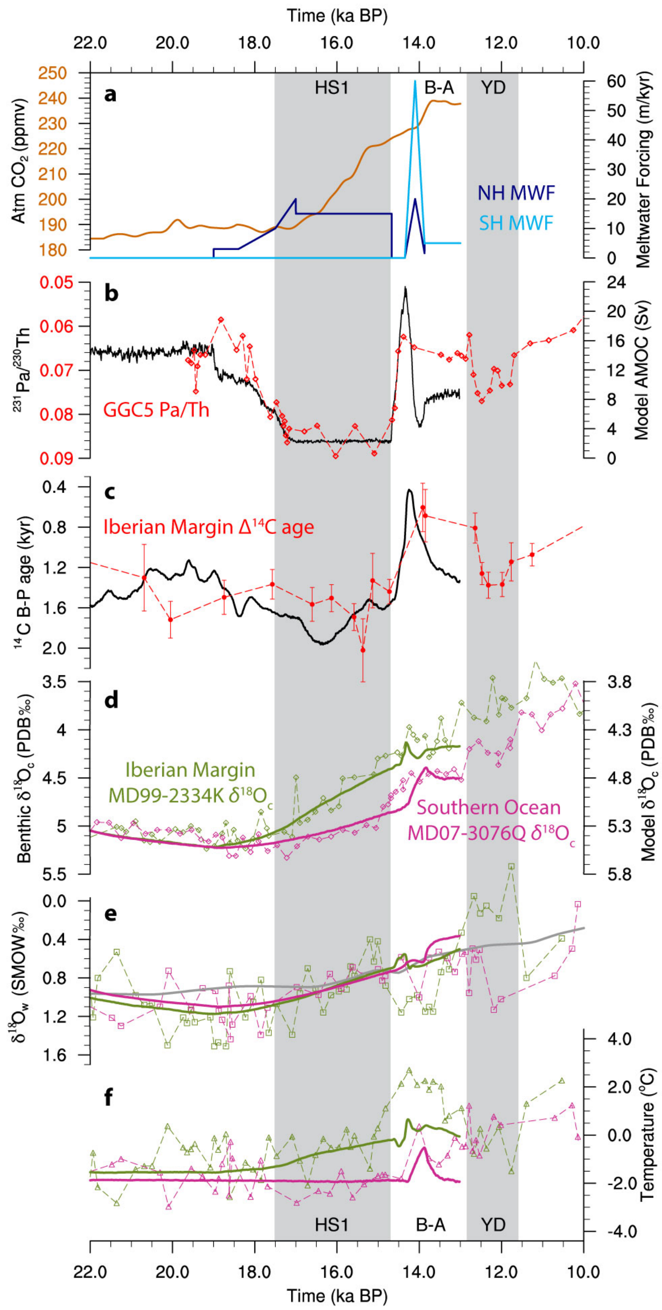

Figure 1.

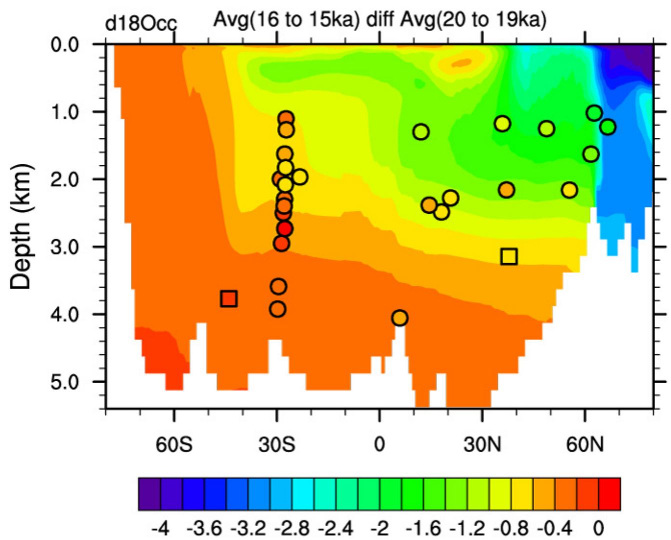
d18Occ
Avg(16 to 15ka) diff Avg(20 to 19ka)
Depth (km)
0.0
1.0
2.0
3.0
4.0
5.0
60S
30S
0
30N
60N
-4 -3.6 -3.2 -2.8 -2.4 -2 -1.6 -1.2 -0.8 -0.4 0

Figure 2.

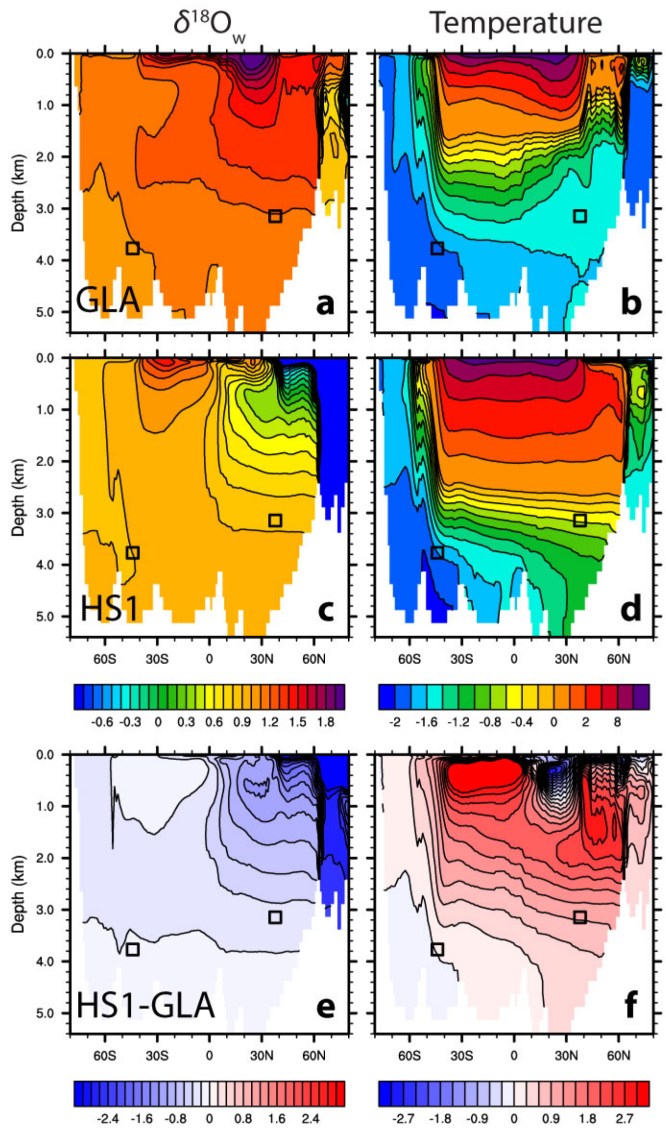
$\delta^{18}O_w$
Temperature
GLA
a
b
HS1
c
d
HS1-GLA
e
f
Depth (km)
0.0
1.0
2.0
3.0
4.0
5.0
60S
30S
0
30N
60N
-0.6 -0.3 0 0.3 0.6 0.9 1.2 1.5 1.8
-2 -1.6 -1.2 -0.8 -0.4 0 2 8
-2.4 -1.6 -0.8 0 0.8 1.6 2.4
-2.7 -1.8 -0.9 0 0.9 1.8 2.7

Figure 3.

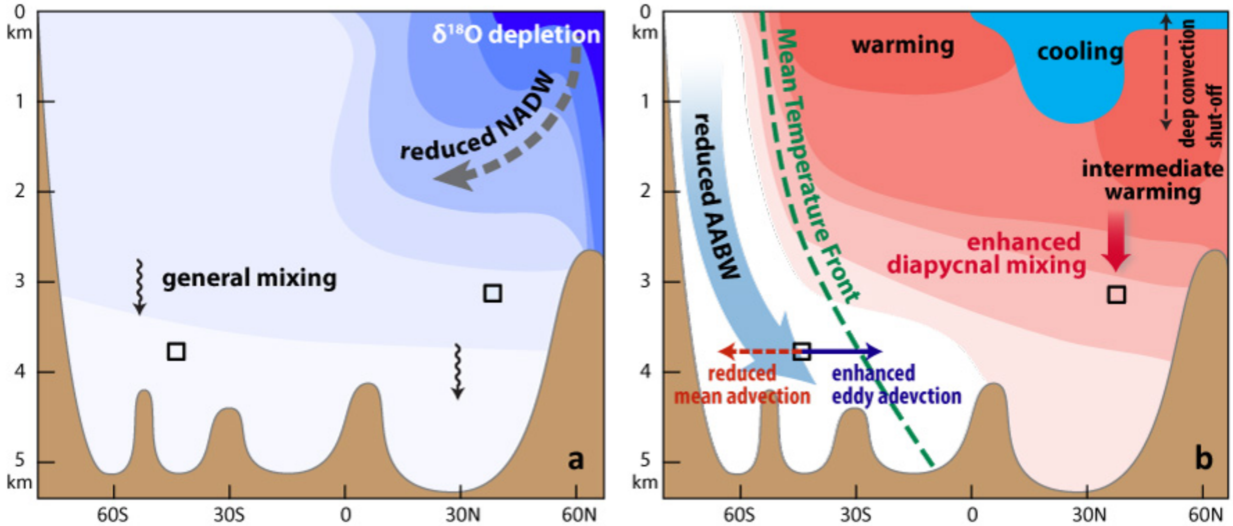
δ18O depletion
reduced NADW
general mixing
a
warming
cooling
deep convection shut-off
Mean Temperature Front
reduced AABW
intermediate warming
enhanced diapycnal mixing
reduced mean advection
enhanced eddy adevction
b
0 km
1
2
3
4
5 km
60S
30S
0
30N
60N

Figure 4.

Methods

POP2 ocean model. The ocean general circulation model used in this research is the Parallel Ocean Program version 2 (POP2)[33], which serves as the ocean component of the Community Earth System Model version 1[34]. POP2 is a primitive equation level-coordinate global ocean model. The horizontal grid of the low resolution version of POP2 increases from 0.8° latitude on the equator to 1.85° at the poles, although the grid is a uniform 3.6° in longitude. There are 60 vertical levels, with 10 m resolution in the upper 200 m, gradually expanding to 250 m resolution below 3000 m depth. Details of the ocean model are given in Danabasoglu et al.[33].

Implemented water isotope and abiotic radiocarbon modules. In the water isotope module, the seawater $\delta^{18}O$ is forced by the isotopic fluxes at the sea surface and advects and diffuses in the ocean interior as a passive tracer. The $\delta^{18}O$ flux is expressed as

$$\begin{aligned} F_\delta &= E(\delta_w - \delta_E) - P(\delta_w - \delta_P) - R(\delta_w - \delta_R) - M(\delta_w - \delta_M) \\ &= (E - P - R - M)\delta_w - (E\delta_E - P\delta_P - R\delta_R - M\delta_M) \end{aligned} \tag{1}$$

where δ_w is the isotopic composition of the surface seawater, which is a globally uniform reference value, δ_E, δ_P, δ_R and δ_M are the isotopic composition of evaporation (E), precipitation (P), river runoff (R) and meltwater from land ice and icebergs (M). It is assumed that there is no isotopic flux during sea ice formation and melting, since the isotopic fractionation in these processes is measured small. The computed F_δ is used in the first layer vertical diffusion term as the tracer boundary condition.

The term $(E - P - R - M)\delta_w$ is the virtual isotopic flux, analogous to the virtual salt flux, representing the diluting effect of the net freshwater flux. The isotopic composition of precipitation

(δ_P) used either observational data or model results. The isotopic composition of runoff (δ_R) used the corresponding local δ_P value as an approximation. The isotopic composition of evaporation (δ_E) is dynamically computed in the model, represented by a simple linear resistance model approach[35].

The abiotic carbon tracers were included in POP2 following the Ocean Carbon Modeling Intercomparison Project protocol[31,36]. This module considers the solubility pump, by which CO_2 is transferred from air to sea by gas exchange as Dissolved Inorganic Carbon (DIC, defined as CO_2 plus bicarbonate and carbonate ions), as the major pathway of atmospheric CO_2 into the ocean. The error by ignoring the biological pump is about 10%[37], because the biological processes affect ^{14}C and ^{12}C compounds in the same manner. A detailed description of the implementation can be found in Jahn et al.[31].

The LGM spin-up and the deglacial transient simulation of iPOP2. The isotope-enabled POP2 was first spun up under LGM conditions (hereafter referred to as the iLGMspin experiment) for 6900 years, with physical spin-up of 900 years and tracer spin-up of 6000 years. The ocean temperature and salinity were initialized from the LGM climatology of TRACE21[16,21]. The momentum boundary condition used the monthly momentum fluxes (τ_x and τ_y) of TRACE21 directly. The heat and freshwater boundary condition adopted a new method, hybrid boundary condition, which was a combination of both flux forcing and surface restoring forcing. In this method, the heat and freshwater fluxes were applied to temperature and salinity fields, with a strong restoring to the TRACE21 surface values applied to both fields at the same time. This allowed more realistic fluxes at the ocean surface and prevented unrealistic feedbacks, especially for the temperature field. The restoring was applied only to the first layer of 10 m, and the restoring time was 10 days and 30 days for temperature and salinity, respectively. The restoring time was set to be longer for salinity to provide a larger deviation at surface, allowing the model to adjust itself to a reasonably stable state[38].

The hybrid boundary condition of this 900-yr physical spin-up used monthly history files for 22.0–21.1 ka of TRACE21. In the following 6000-yr tracer spin-up, the hybrid boundary condition used the 22.0–20.0 ka historical files of TRACE21, and looped the 2000-yr data for three times. In the subsequent deglacial transient simulation of the iPOP2 (hereafter referred to as the iPOP2-TRACE experiment), the surface variables used in the hybrid boundary condition were taken from TRACE21 every month at the corresponding time.

The water $\delta^{18}O$ was initialized at zero at the beginning of iLGMspin. The boundary condition for $\delta^{18}O$ was taken from 24 isoCAM3 paleoclimate snapshot simulations during the last 21,000 years[39]. The isotopic snapshot simulations used the physical setups the same as in the TRACE21 simulation. 22 of them were 1000 years apart from 21 ka to present, and two additional were at the B-A and Younger Dryas when climate changed abruptly. Each snapshot experiment was forced by the same external forcing as for TRACE21 and had a length of 50 years. The mean of the last 30 years was used in the iPOP2-TRACE simulation. Since the hybrid boundary condition was applied for the ocean surface salinity, an artificial freshwater flux corresponding to the restoring term was introduced to the ocean. In terms of $\delta^{18}O$ surface flux, we considered no fractionation effect related to this artificial flux, but only its dilution effect. That was, the freshwater flux corresponding to the restoring term was only included in the virtual flux (the first term of Eq. 1). Starting from 19 ka, additional meltwater fluxes were added to the ocean model, mimicking the meltwater discharges into the surface ocean (specific volume and locations at each period are described in He[21]). In the Northern Hemisphere, the isotopic composition of meltwater is prescribed by its characteristic glacial value of −31‰[40]. In the Southern Hemisphere, meltwater discharge was prescribed to the Ross Sea and the Weddell Sea starting from 14.35 ka, and an isotopic value of −38‰ was assigned to it. This value was determined based on the 14 ka $\delta^{18}O$ values of close-to-shore TALDICE[41] and Taylor Dome[42] ice cores.

In iLGMspin, the abiotic $\Delta^{14}C$ was initialized from its modern values of a 6000-yr iPOP2 modern simulation[31], before being spun-up for another 6000 years with the other tracers for LGM conditions. In iPOP2-TRACE, the atmospheric CO_2 and $\Delta^{14}C$ values were prescribed as the boundary condition for the radiocarbon module. The atmospheric CO_2 concentration was fixed at 185 ppm for iLGMspin, then ramped following the reconstruction curve used in Joos and Spahni[43], the same as what was used in TRACE21. The atmospheric $\Delta^{14}C$ was fixed at 450‰ for iLGMspin, then gradually decreased following the IntCal09 reconstruction[44].

Computing $\delta^{18}O_c$ from seawater $\delta^{18}O_w$ and temperature. Precise interpretation of the $\delta^{18}O_c$ record requires separating the two independent components (seawater $\delta^{18}O_w$ and temperature). It remains a challenge in proxy reconstruction but is easy to achieve in modeling, since transient evolutions of the two components at available core locations are simulated directly in the iPOP2-TRACE experiment. For shallow locations where temperatures are above 5°C, benthic $\delta^{18}O_c$ are estimated by the following formula[45]

$$\delta^{18}\mathrm{O}_{\mathrm{c(PDB)}} = \delta^{18}\mathrm{O}_{\mathrm{w(SMOW)}} - \sqrt{310.6 + 10T} + 21.9 - 0.27 \qquad (2)$$

where T is the water temperature in °C, and 0.27 is the conversion factor between the PDB standard and the SMOW standard[46]. While for deep locations where temperature are below 5°C, the $\delta^{18}O_c$ is more linearly depend on temperature. Therefore benthic $\delta^{18}O_c$ are estimated by a different formula[23,45]

$$\delta^{18}\mathrm{O}_{\mathrm{c(PDB)}} = \delta^{18}\mathrm{O}_{\mathrm{w(SMOW)}} - 0.27 + \frac{16.9 - T}{4} \qquad (3)$$

In this way, the time series of benthic $\delta^{18}O_c$ and its two components ($\delta^{18}O_w$ and temperature) can be explored separately.

Understanding the $\delta^{18}O_c$ early post-glacial (22-19ka) increase. The early post-glacial increasing trend of $\delta^{18}O_c$ is caused by the increase of water $\delta^{18}O_w$ (Fig. 1e), since the water temperature remained unchanged during this period (Fig. 1f). When land ice sheets reached their maximum expansion at the LGM, light water isotopes stopped accumulating on land in the form of ice, resulting in maximum $\delta^{18}O_w$ enrichment in the ocean. The enrichment is not simultaneous throughout the global ocean but peaks sequentially from the top to bottom layers and across different ocean basins well beyond the LGM[47,5] (Supplementary Fig. 6), due to the long overturning time-scale from ~1500 yr in the Atlantic to more than 3000 yr in the Pacific.

Transient tracer simulations with circulation fixed at 19 ka (iPOP2-19ka) and present (iPOP2-0ka). To gain a deeper understanding of the impact of circulation on the deglacial water isotope distribution, we would need to separate the circulation effect from other surface flux changes of water isotopes. This was achieved by two sensitivity experiments. One was iPOP2-19ka, which simulated the water isotope tracers with transient surface forcing, but held the AMOC at the 19 ka level. To maintain the 19 ka AMOC, the hybrid boundary condition of physical environment used 1,000 years of monthly historical files of 20.0–19.0 ka of TRACE21, and looped the 1,000-yr data until reaching 16 ka. The other experiment iPOP2-0ka was similar as iPOP2-19ka, but with a modern AMOC. Its modern AMOC was maintained by forcing the iPOP2 with the interannual forcing (IAF) from the CLIVAR Working Group on Ocean Model Development

(WGOMD) Coordinated Ocean-ice Reference Experiments (CORE), which is referred as CORE-IAF.v2[48]. In both experiments, the water isotope tracer boundary condition was taken from the monthly output of tracer fluxes in iPOP2-TRACE. The use of the tracer boundary condition of iPOP2-TRACE assured that the tracer flux through the surface in iPOP2-19ka was exactly the same, but followed a different circulation pattern after entering the ocean interior.

When the strength of AMOC is held at its 19 ka level of ~15 Sv (Sv ≡ 10^6 m^3 s^{-1}; Supplementary Fig. 1a) in iPOP2-19ka, the low-^{18}O signal is no longer able to accumulate in the upper NA during HS1 as in iPOP2-TRACE (Fig. 3e). Instead, that signal is better distributed in the whole Atlantic and even to the Pacific and Indian Ocean (Supplementary Fig. 9b). This distribution pattern confirms that the slowdown of AMOC is indeed the cause of the accumulation of ^{18}O-depleted water in the upper layers of the NA in iPOP2-TRACE.

It is also noted that the tongue of the southward expansion of the ^{18}O-depleted water is confined above 3000 m in iPOP2-19ka (Supplementary Fig. 9b), even with a strong and fully functional AMOC. This is because the NADW is confined above the thick abyssal layer of AABW at 19ka, and cannot deepen (Supplementary Fig. 2d). In contrast, the expansion of the low-^{18}O tongue in iPOP2-0ka reaches as deep as 4000 m in the NA (Supplementary Fig. 9c), consistent with its deep expanded NADW at 4000 m level (Supplementary Fig. 2b). This confirms that the water isotope tracer distribution below the ocean upper layers is mostly determined by the circulation pattern, namely the AMOC structure.

Sensitivity tracers $\delta^{18}O_w$–MWF and $\delta^{18}O_w$–Hydro. The δ^{18}O surface flux forcing (eq. 1) can be grouped into two parts; meltwater forcing (*M*), which is also known as the volume effect, and hydrographic forcing, which includes evaporation (*E*), precipitation (*P*), and river runoff (*R*). To explore the relative contributions of the two parts during the early deglaciation, we implemented two sensitivity tracers in the iPOP2-TRACE simulation after 19 ka. One was $\delta^{18}O_w$–MWF, which followed the transient meltwater forcing, but its hydrographic forcing was kept as in 19 ka. The other was $\delta^{18}O_w$–Hydro, which followed the transient hydrographic forcing with no meltwater forcing.

The evolution of $\delta^{18}O_w$–MWF indicates that the volume effect is the major cause of the $\delta^{18}O_w$ depletion at both core locations, and itself would result in a greater magnitude and a mild lead of the depletion of the northern core (Supplementary Fig. 8b). However, $\delta^{18}O_w$–Hydro indicates the hydrographic forcing causes an enrichment of the northern core and does not impact the southern core much, therefore opposing the volume effect (Supplementary Fig. 8c). The relative contributions can be seen clearly in the Atlantic zonal mean changes of the two sensitivity tracers. The $\delta^{18}O_w$–MWF highly represents the pattern of $\delta^{18}O_w$ changes, but with a slight greater magnitude (Supplementary Fig. 9d). The $\delta^{18}O_w$–Hydro exhibits enrichment over the whole basin with greatest magnitude at 0–30°N near surface (Supplementary Fig. 9e), because of a small isotopic fractionation factor (liquid to vapor) in evaporation at a warming scenario.

The timing of the meltwater pulse 1A. One feature of the SO $\delta^{18}O_c$ record is the sharp decrease at the HS1/B-A boundary (Fig. 1d). The same sharp $\delta^{18}O_c$ decrease is simulated by our model, but apparently lags the reconstruction. The lag of the model occurs because the meltwater over the SO mimicking the meltwater pulse 1A (MWP-1A) was prescribed after the Bølling warming event[16,21]. As the chronology and origin of the MWP-1A and its temporal relationship with the Bølling warming all remain debatable[49], the sharp and lagged $\delta^{18}O_c$ decrease in our simulation suggests the timing of the MWP-1A should be no later than the Bølling warming[50,51], and a significant portion of the meltwater should originate from the Antarctic Ice Sheet[52].

The compensation effect of seawater $\delta^{18}O_w$ and temperature at the start of B-A. Indeed, the deep temperature response also played an interesting role in the muted response of $\delta^{18}O_c$ in the subsequent B-A warming (~14.67 to 14.35 ka). During this period, the northern-sourced water formation was reactivated dramatically[16,21], as shown in consistent sharp evolution of multiple geotracers in both reconstruction and the model (Fig. 1). There was, however, little change in $\delta^{18}O_c$ in the deep NA, because the low $\delta^{18}O_w$ water brought by the NADW from the surface was compensated by the accompanying surface cooling that was also brought to the depth (Fig. 1d to f).

Such compensation effect is more obvious at NA intermediate core locations during this time interval. Both $\delta^{18}O_c$ at core locations NA87-22 (55.5°N, 2161 m)[53,54] and MD95-2037 (37.1°N, 2156 m)[55,56] reached their plateau after the fast HS1 decreases (Supplementary Fig. 10b and c). A decomposition of the water isotope component and temperature component clearly shows that both components contributed to the $\delta^{18}O_c$ HS1 decreases, but compensated with each other at the start of B-A (Supplementary Fig. 10f and g). When the AMOC recovered at the start of B-A, $\delta^{18}O_w$ experienced a sudden decrease since ^{18}O-depleted water was brought from the high latitudes, while temperature experienced a sudden drop since the cold anomaly was brought from the surface. After the impulses of anomalous $\delta^{18}O_w$ and temperature passed by, the two components returned to their pre-B-A condition (with a mild overshooting of $\delta^{18}O_w$), leading to a small increase of the $\delta^{18}O_c$.

Tracer budget analysis. The deep ocean $\delta^{18}O_w$ and heat budget analysis is based on the tracer transport equation

$$\frac{\partial T}{\partial t} = -u\frac{\partial T}{\partial x} - v\frac{\partial T}{\partial y} - w\frac{\partial T}{\partial z} + M_{\mathrm{H}}(T) + M_{\mathrm{V}}(T) \tag{4}$$

where the tracer tendency is influenced by, from left to right, zonal advection, meridional advection, vertical advection, horizontal mixing, and vertical mixing. The three advection terms together are called mean advection, which represents the advective fluxes due to the resolved mean flow, is estimated by a second-order centered discretization form based on the mean velocity. Vertical mixing, also referred to as diapycnal mixing, is given by

$$M_{\mathrm{V}}(T) = \delta_z(\kappa\delta_z T) \tag{5}$$

where κ is the diapycnal mixing coefficient and is spatially variant. This term is estimated by a finite-difference discretization form based on κ. Horizontal mixing is computed by Gent-McWilliams parameterization[57] in the model, which includes along-isopycnal mixing and eddy-induced advection. Since it is not a standard output and there is no off-line scheme to directly estimate it, we use the residual term to represent the horizontal mixing

$$M_{\mathrm{H}}(T) = \frac{\partial T}{\partial t} + u\frac{\partial T}{\partial x} + v\frac{\partial T}{\partial y} + w\frac{\partial T}{\partial z} - M_{\mathrm{V}}(T) \tag{6}$$

It is a good representation in the deep ocean where high-frequency noises are small. All estimates are based on the decadal mean outputs.

The tracer budget analysis was performed at two deep Atlantic regions: i) 30-40°N, 30°W to eastern coast of NA at the 3133 m layer, which includes the MD99-2334K core location, and ii) 36-46°S of Atlantic at the 3628 m layer, which includes the MD07-3076Q core location (Supplementary Fig. 11a). The dominant terms of $\delta^{18}O_w$ balance change from horizontal advection terms during the LGM, to diapycnal mixing and upwelling during HS1, but the sign of mixing and upwelling reverses in the transition (Supplementary Fig. 11b). This occurs because the surface meltwater is so ^{18}O-depleted that the vertical gradient of $\delta^{18}O_w$ is reversed from top enrichment to top depletion from the LGM to HS1 (Fig. 3a and c). This is different from temperature whose vertical gradient always remains stable for the whole water column due to convective stability requirement, except for at the very thin top layer (where cooling is compensated by extremely fresh water; Fig. 3b and d). Therefore, the surface source of depleted $\delta^{18}O_w$ is mostly confined at top layers and diluted downward slowly by reduced NADW and mixing, leaving only a modest depletion in the deep NA.

The heat budget analysis, instead, shows that the temperature field involves dynamic response, which is much more efficient than the passive tracer response of $\delta^{18}O_w$ and is able to heat the deep NA more directly. In the deep NA, the dominant balance changes from between zonal advection and meridional advection during the LGM, to between vertical diapycnal mixing and vertical advection (upwelling) during HS1 (Supplementary Fig. 12b). The vertical diapycnal mixing brings heat from intermediate depth to the deep ocean, and overwhelms the cooling effect of upwelling, causing this region to warm during HS1. The intermediate warming center at 1500 m in the NA results from 1) the cessation of deep convection which used to bring warm water up to surface, 2) protection by the meltwater at surface from intense atmospheric cooling, and 3) continuous heat transport from tropics and subtropics[30]. The NA warming center was 1000 m deeper than the warming center in the South Atlantic (Fig. 3f). It is therefore more efficient for the diapycnal mixing to bring the warmth down in the NA than in the South Atlantic, causing strong warming in the north and weak warming in the south.

The heat budget at the SO region, instead, features a strong horizontal mixing during the LGM (Supplementary Fig. 12c). The dominant component of the horizontal mixing is the eddy-induced advection, since this region is the mean temperature front where isotherms are strongly tilted. During HS1, the cooling effect of the northward advection decreases due to a reduced AABW formation, tending to leave this region warm. However, the mean advection/eddy advection balance is so strong that this tendency is mostly canceled by the enhanced cold eddy advection. Therefore, the deep temperature change to the south of the mean temperature front is small.

Other model-data comparisons on the Atlantic deglacial $\delta^{18}O_c$. We made a model-data comparison for a $\delta^{18}O_c$ transect near the Brazil Margin in the South Atlantic[4] below 1000 m (Supplementary Fig. 4; core information is in Supplementary Table 1). The model successfully reproduces the Hovmoller diagram of the observed deglacial $\delta^{18}O_c$ evolution with respect to both pattern and magnitude. Both the observations and model show that $\delta^{18}O_c$ of upper depths (above 2500 m) started to decrease at 18 ka, but that of lower depths (below 2500 m) remained unchanged until about 15 ka. Therefore, the upper-depth depletion led the lower-depth depletion by about 3000 years. Lund et al.[4] attribute the late lower-depth $\delta^{18}O_c$ changes to the late onset of the deep water $\delta^{18}O_w$ decrease. However, our model shows that the $\delta^{18}O_w$ at 28°S decreased with similar magnitudes at each level during HS1 (Fig. 3e). Instead, the warming at 28°S was uneven, with much larger warming at upper depths and smaller warming at lower depths (Fig. 3f). A heat budget analysis performed at this location (not shown here) suggests that diapycnal mixing brought the heat at upper levels down, forming an increased vertical temperature gradient.

We also compare the model simulated $\delta^{18}O_c$ with four regional benthic $\delta^{18}O_c$ stacks in the Atlantic, each with independent radiocarbon age models[47] (Supplementary Fig. 5a). The four regional stacks sampled cores at intermediate (1000–2000 m) and deep (below 2000 m) sites in both the NA and SA. By defining the termination onset as the first $\delta^{18}O_c$ point that is at least 0.1‰ lighter than the maximum $\delta^{18}O_c$ value[47], the model $\delta^{18}O_c$ indicates an earlier termination onset age at the intermediate depth than in the deep ocean, which is consistent with what the observed stacks indicate. However, there are two notable differences between the model and the observed stacks. First, the decreases of the intermediate stacks are much greater than those of the deep ones in the model, whereas this difference in magnitude is small in the observations. Second, the model identifies a later termination onset and a smaller decrease during HS1 in the deep SA stack than in the deep NA, which is not found in the observations. Some of the differences may reflect assumptions used in constructing the radiocarbon age models of the stacks, particularly the assumption of a constant reservoir age.

Based on the model-data consistencies at single core sites instead of stacks, we confirm the recent realization that the use of $\delta^{18}O_c$ as a stratigraphic tool is problematic[4,5], since the timing of $\delta^{18}O_c$ changes across a range of depths varies by hundreds or even thousands of years (Supplementary Fig. 5b). This asynchrony also implies that correcting deep $\delta^{18}O_c$ records for changes in global ice volume by using a global/regional $\delta^{18}O_c$ stack[47,58,59] is likely inaccurate, as the meltwater-induced $\delta^{18}O_w$ signals and local temperature changes are highly location dependent. Accurate interpretation of the $\delta^{18}O_c$ records therefore requires benthic foraminiferal records paired with temperature proxies, independent age models, and independent evidence from modeling efforts.

Data Availability. The sources of the observed data are listed in the Supplementary Table 1. The model data are stored on the High Performance Storage System at NCAR.

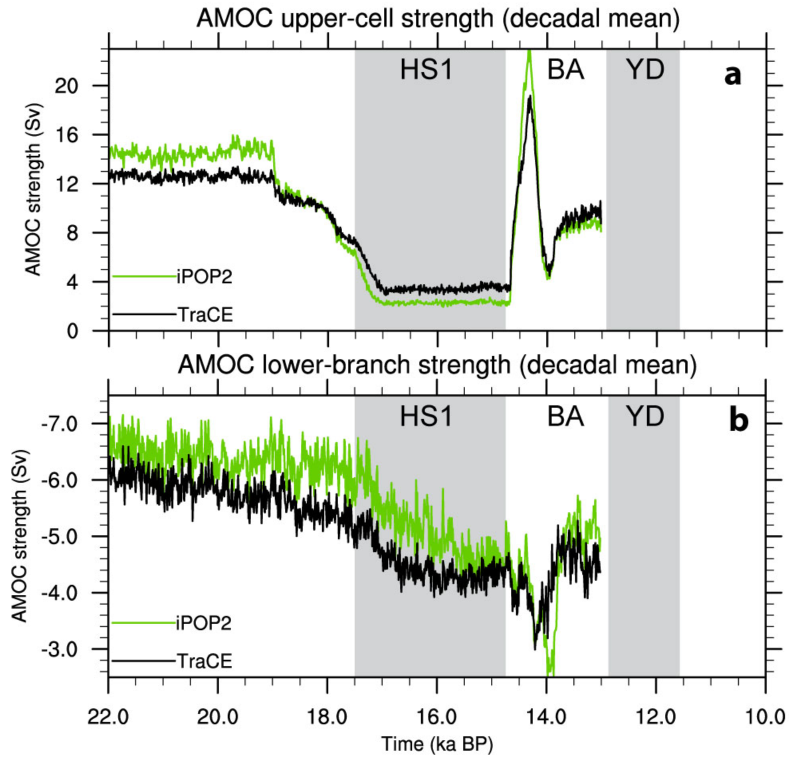

Supplementary Figure 1 | Changes of AMOC strength in the iPOP2-TRACE and TRACE21 simulations. a, iPOP2-TRACE (green) AMOC strength of the upper cell compare with that of TRACE21 (black). **b**, Same as (**a**), but for the AMOC abyssal cell, which is defined as the minimum AMOC transport in the Southern Atlantic below 2000 m. Negative values indicate counterclockwise circulation.

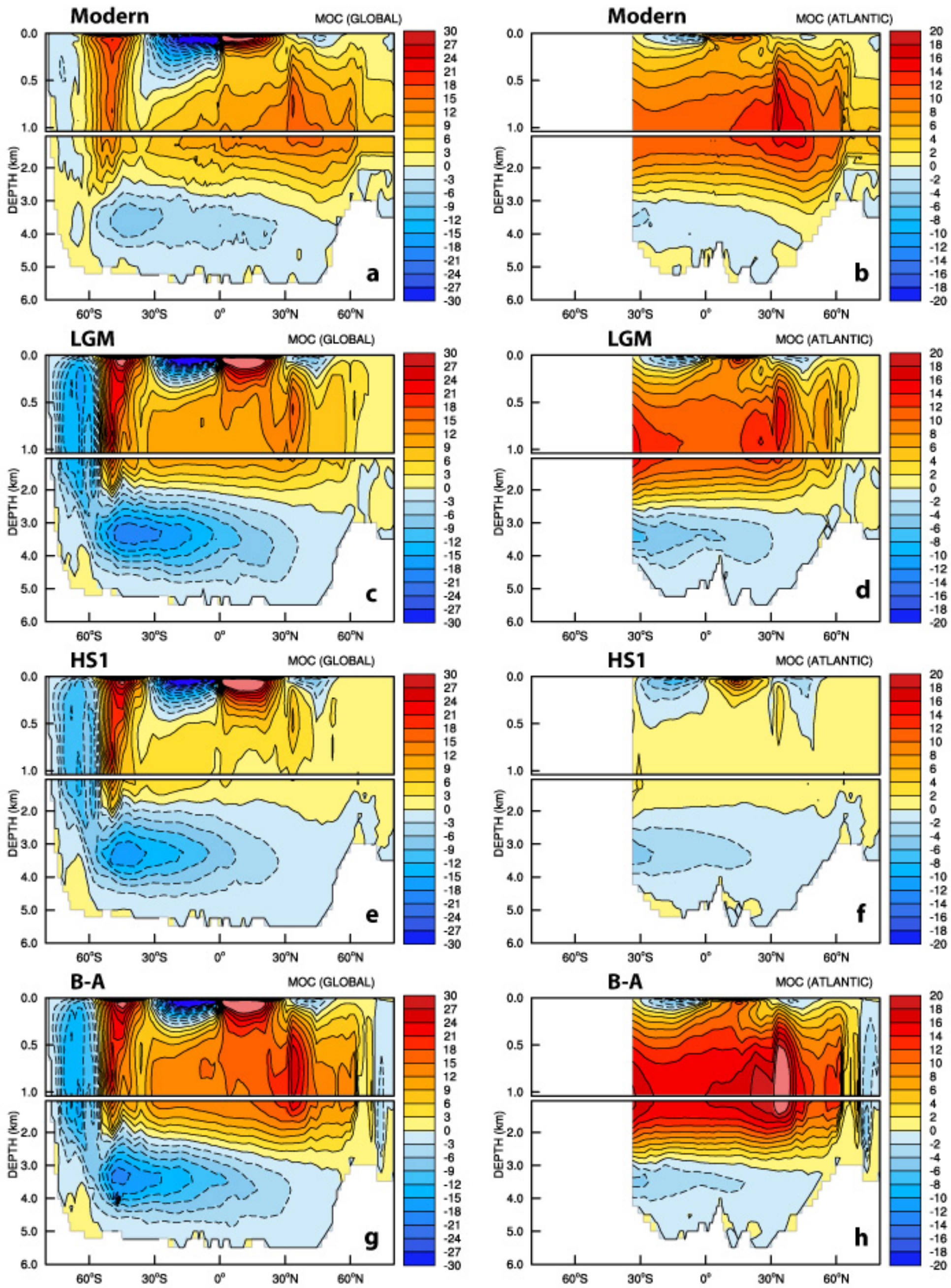

Supplementary Figure 2 | Global (left) and Atlantic (right) total circulation at (a-b) modern, (c-d) glacial at 19 ka, (e-f) HS1 at 16 ka, and (g-h) B-A at 14.35 ka. Total circulation is defined as the sum of the Euler mean circulation and the circulation caused by meso-scale eddies (submeso-scale eddies are ignored since they are small and concentrated at surface layers). Total circulation is directly related to tracer transport.

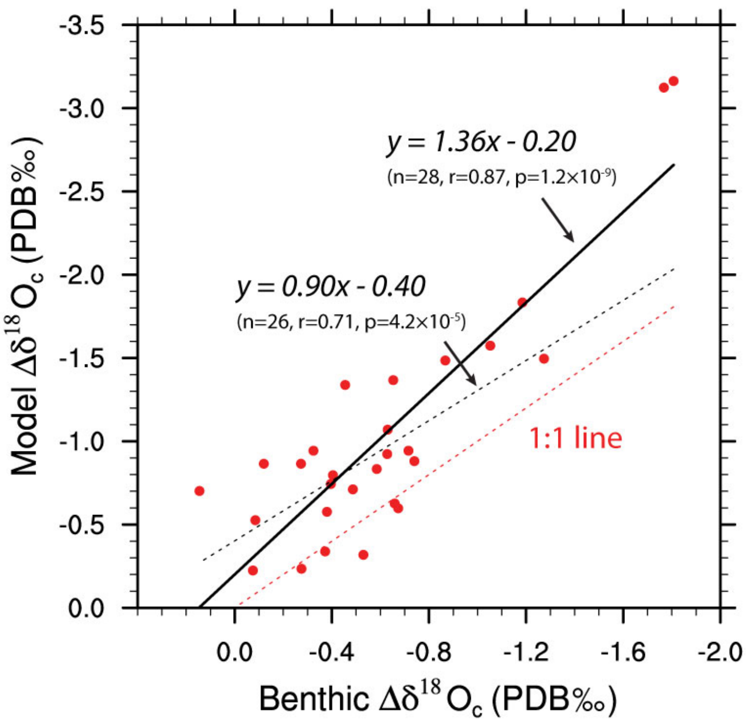

Supplementary Figure 3 | Correlation between measured benthic $\delta^{18}O_c$ changes and model outputs from grid cells closest to core locations. The geographic locations of the 28 Atlantic cores are shown in Fig. 2 and listed in Supplementary Table 1. The black dash and solid lines are regressions with and without the two cores of large $\delta^{18}O_c$ decreases (the two dots in the upper right corner). In both cases, high correlations (0.87 and 0.71) are found between the model and observation.

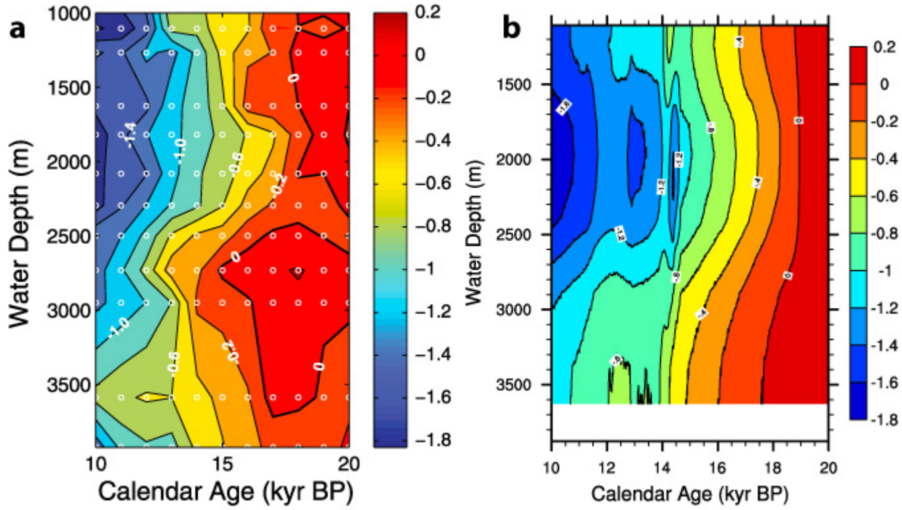

Supplementary Figure 4 | Model-data comparisons for $\delta^{18}O_c$ transect near the Brazil Margin in the South Atlantic. a, Hovmöller diagram of $\delta^{18}O_c$ anomalies for the 10-20 kyr B.P. time interval. Anomalies are the stable isotope value at each water depth minus the mean LGM value (19-23 kyr B.P.) at that depth. Figure is from Fig. 8 of Lund et al.[4]. **b**, Model hovmöller diagram at the same location as in (**a**). The model results reproduce the proxies both in pattern and magnitude. Both show upper depths $\delta^{18}O_c$ started to decrease much earlier than lower depths.

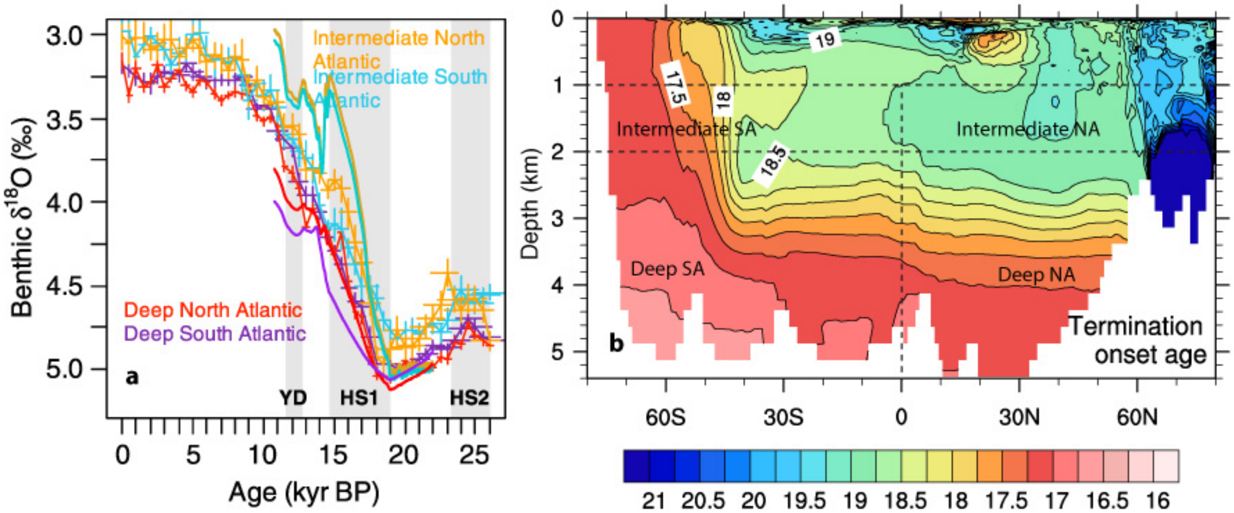

Supplementary Figure 5 | $\delta^{18}O_c$ indicated termination onset age. a, Model $\delta^{18}O_c$ compares with Atlantic regional benthic $\delta^{18}O_c$ stacks[47] for the last deglaciation. The lines with error bars are the stacks at four regions, indicated by different colors and noted in the figure (from Fig. 5 of Stern et al.[47]). Error bars show the 95% age uncertainty and ±1 standard error for stacked $\delta^{18}O_c$ values. Solid lines are the model results, sampling at the same core cites as the stacks do. **b**, Model simulated age (kyr B.P.) of the termination onset, which is defined as the first $\delta^{18}O_c$ point that is at least 0.1‰ lighter than the maximum $\delta^{18}O_c$ value[47]. Dash lines indicate the four regions as defined in (**a**).

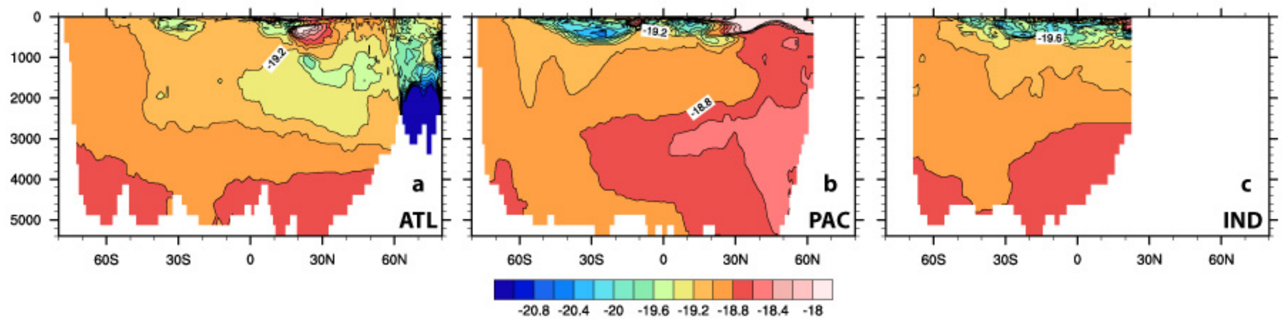

Supplementary Figure 6 | Zonally averaged timing of maximum $\delta^{18}O_c$ at (a) Atlantic, (b) Pacific, and (c) Indian Ocean basins. Maximum values are generally reached first at upper ocean layers, then at intermediate and deep ocean. The deep North Pacific is found to be the region which reached its local maximum $\delta^{18}O_c$ latest (after 18.6 ka).

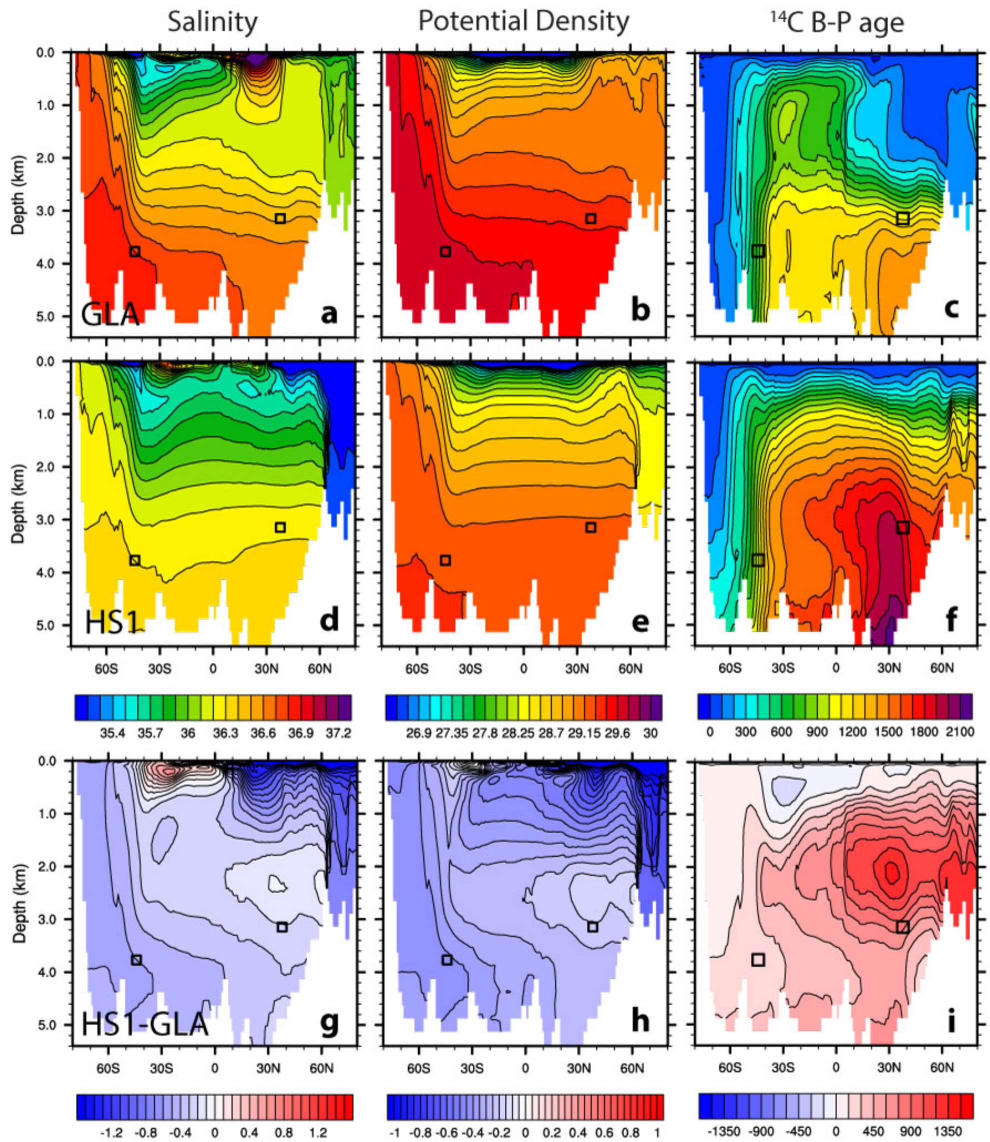

Supplementary Figure 7 | Similar as Figure 3, but for salinity (left), potential density (middle) and radiocarbon benthic-planktonic age offset (right).

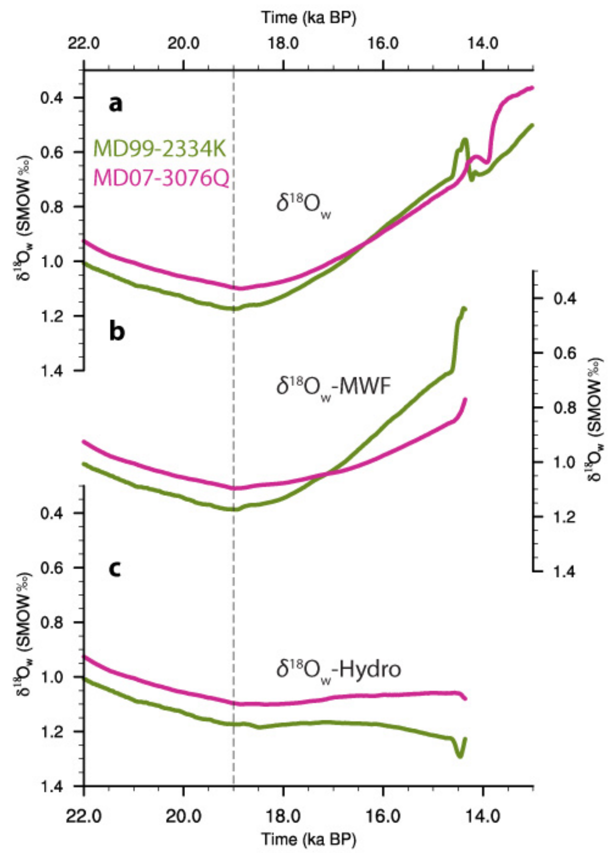

Supplementary Figure 8 | Standard $\delta^{18}O_w$ and two sensitivity tracers at the two deep Atlantic core sites. **a**, Simulated $\delta^{18}O_w$ at Iberian Margin (MD99-2334K, green) and Southern Ocean (MD07-3076Q, pink) sites as in Fig. 1e. **b**, Sensitivity tracer $\delta^{18}O$-MWF, which is forced by the transient meltwater $\delta^{18}O$ forcing and fixed surface hydrographic forcing of 19 ka. **c**, Sensitivity tracer $\delta^{18}O$-Hydro, which is forced by the transient surface hydrographic forcing and no meltwater $\delta^{18}O$ forcing.

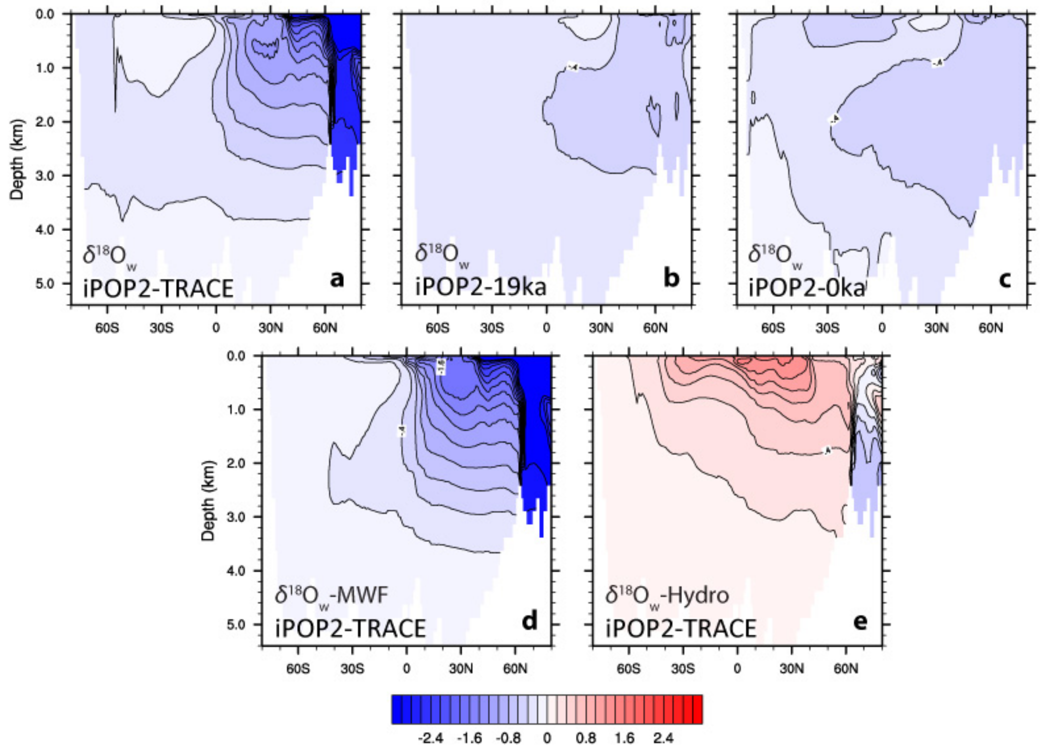

Supplementary Figure 9 | Atlantic zonally averaged $\delta^{18}O_w$ changes in the standard and sensitivity experiments. a-c, Standard experiment iPOP2-TRACE (**a**), as in Fig. 3e, sensitivity experiment iPOP2-19ka (**b**), and sensitivity experiment iPOP2-0ka (**c**). Atlantic zonally averaged changes are also shown for two sensitivity tracers $\delta^{18}O$-MWF (**d**) and $\delta^{18}O$-Hydro (**e**) in the control experiment. Refer to Methods for experiment and tracer details. All the changes were computed as the differences between 16 ka and 19 ka in each experiment.

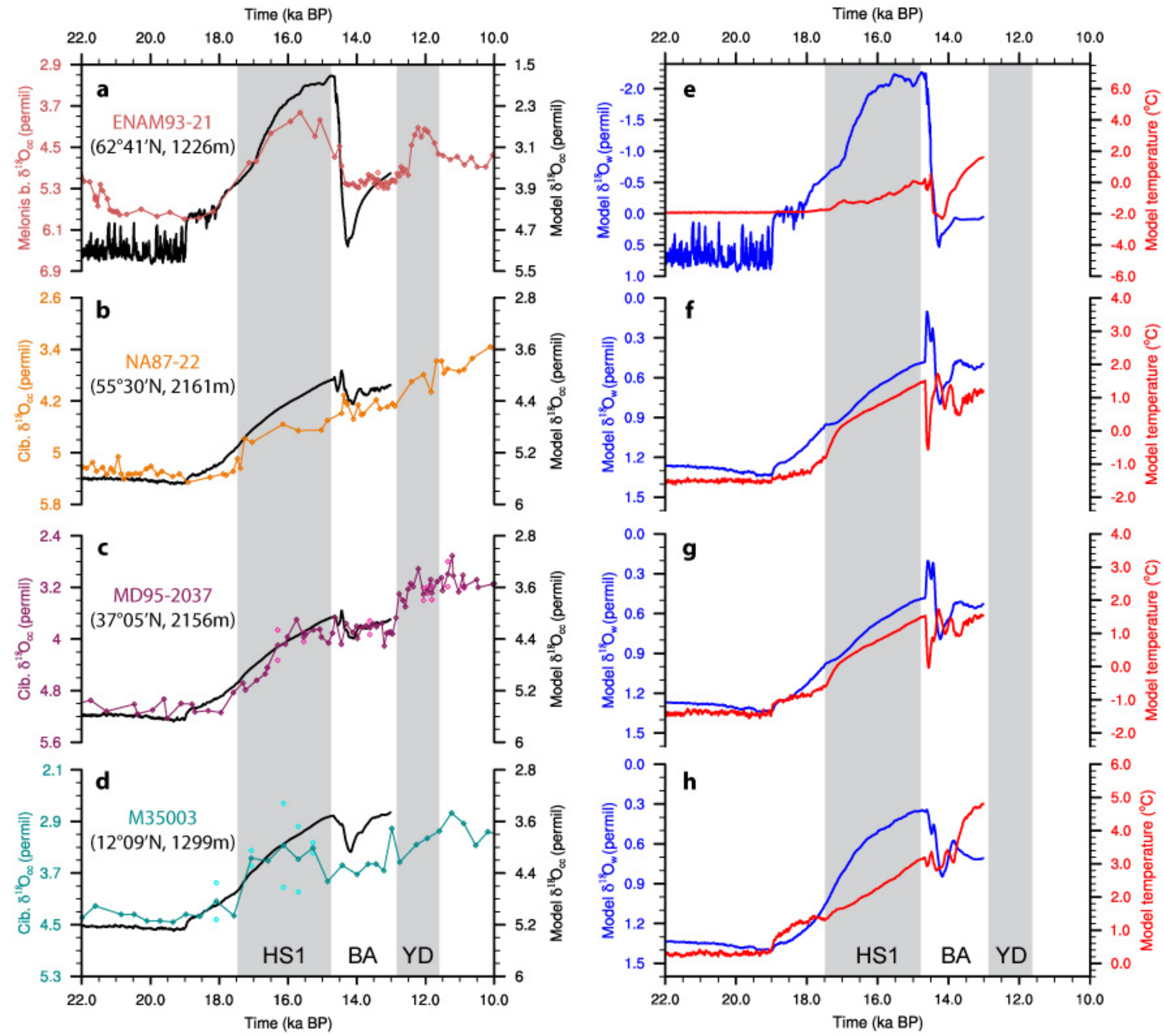

Supplementary Figure 10 | Model-data comparison for mid-depth $\delta^{18}O_c$ records. a-d, Norwegian Sea and North Atlantic benthic $\delta^{18}O_c$ records from the 1000-2200 m depth range, and model $\delta^{18}O_c$ (black) at the corresponding sites. Complete references for the isotopic measurements and age models of the $\delta^{18}O_c$ records are summarized in Waelbroeck et al.[5]. **e-h**, Simulated water $\delta^{18}O_w$ (blue) and temperature (red) at each site as indicated on the left panel.

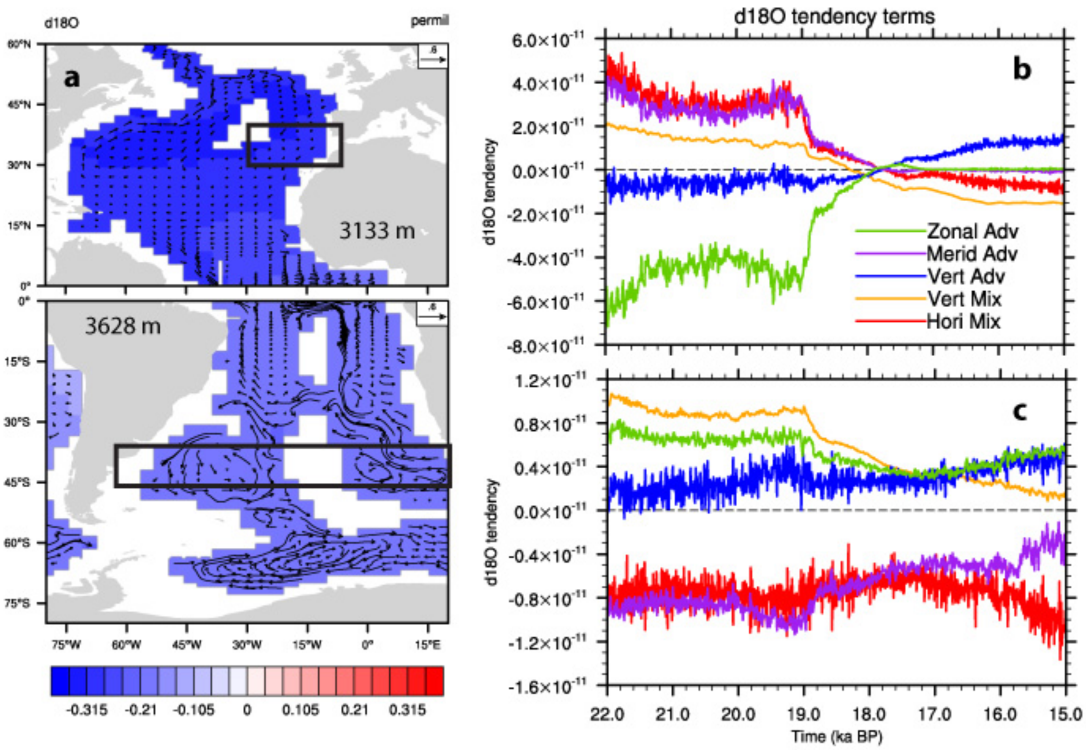

Supplementary Figure 11 | $\delta^{18}O_w$ tracer budget analysis at selected deep Atlantic regions. **a**, $\delta^{18}O_w$ changes (colors) at 3133 m in the North Atlantic and 3628 m in the South Atlantic between 16 ka and 19 ka. Vectors are horizontal mean flow at 16 ka. Two black boxes indicate the regions where tracer budget analysis is performed. **b-c**, Time series of area averaged tendency terms in each box region. Details of each term can be found in Methods.

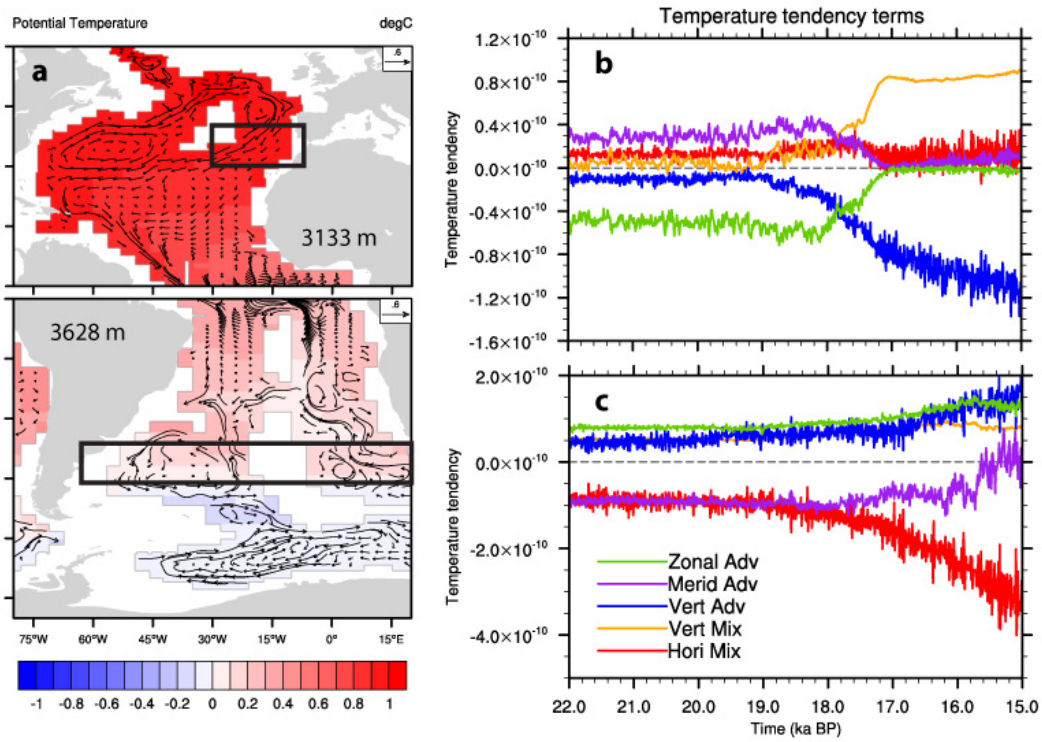

Supplementary Figure 12 | Same as Supplementary Fig. 11, but for heat budget analysis. Vectors in (**a**) are horizontal mean flow at 19 ka.

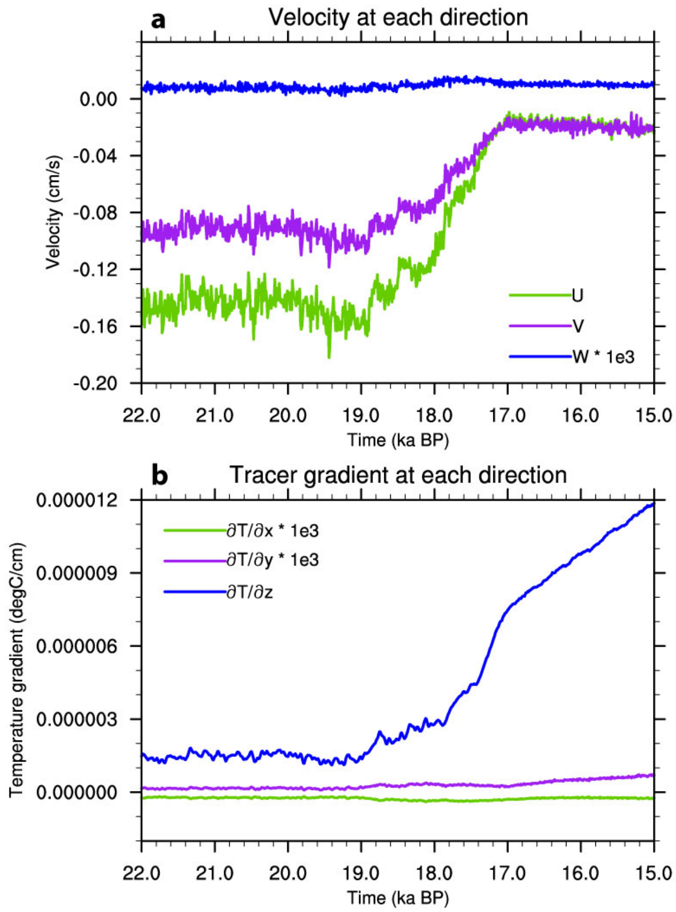

Supplementary Figure 13 | Breakdown of the three mean advection terms of Supplementary Figure 12 into (**a**) mean velocities and (**b**) temperature gradients. Zonal, meridional, and vertical directions are represented by green, purple and blue. The vertical velocity in (**a**) and two horizontal temperature gradients in (**b**) are enlarged by 1000 times in order for comparison. The vertical velocity does not change much as the horizontal velocities do after 19 ka. Instead, the vertical temperature gradient has a marked increase.

Supplementary Table 1

List of benthic $\delta^{18}O_c$ cores used in Fig. 2. All cores are below 1000 m depth and have dated data during both the glacial period (20.0-19.0 ka) and late HS1 (16.0-15.0 ka).

Core	Latitude	Longitude	Depth (m)
MD95-2010[60]	66.68	-4.57	1226
ENAM93-21[61,62]	62.74	-4	1020
EW9302-24GGC[3]	61.76	-21.67	1629
NA87-22[53,54]	55.5	-14.7	2161
EW9302-2JPC[63]	48.8	-45.08	1251
MD99-2334K[6,27]	37.8	-10.17	3146
MD95-2037[55,56]	37.09	-32.03	2159
MD99-2339[64]	35.89	-7.53	1177
GeoB7920-2[65,66]	20.75	-18.58	2278
GIK13289-2[67]	18.07	-18.01	2485
GeoB9508-5[68]	14.5	-17.95	2384
M35003-4[69–71]	12.09	-61.24	1299
EW9209-1JPC[72,73]	5.91	-44.2	4056
GeoB1711[74,75]	-23.32	12.38	1967
KNR159-5-90GGC[4,25]	-27.35	-46.63	1105
KNR159-5-36GGC[25,76]	-27.27	-46.47	1268
KNR159-5-17JPC[77]	-27.7	-46.49	1627
KNR159-5-78GGC[77]	-27.48	-46.33	1829
KNR159-5-33GGC[77]	-27.56	-46.19	2082
KNR159-5-42JPC[25,78]	-27.76	-46.63	2296
KNR159-5-73GGC[3]	-27.89	-46.04	2397
KNR159-5-30GGC[77]	-28.13	-46.07	2500
KNR159-5-63GGC[4]	-27.7	-46.5	2732
KNR159-5-20JPC[4]	-28.64	-45.54	2951
KNR159-5-125GGC[78]	-29.53	-45.08	3589
KNR159-5-22GGC[78]	-29.78	-43.58	3924
GeoB1720-2[79]	-29	13.84	1997
MD07-3076Q[2,5]	-44.07	-14.21	3770

References

1. Broecker, W. S., Peng, T.-H., Trumbore, S., Bonani, G. & Wolfli, W. The distribution of radiocarbon in the glacial ocean. *Global Biogeochem. Cycles* **4,** 103–117 (1990).
2. Skinner, L. C., Fallon, S., Waelbroeck, C., Michel, E. & Barker, S. Ventilation of the deep Southern Ocean and deglacial CO_2 rise. *Science* **328,** 1147–51 (2010).
3. Oppo, D. W., Curry, W. B. & McManus, J. F. What do benthic $\delta^{13}C$ and $\delta^{18}O$ data tell us about Atlantic circulation during Heinrich Stadial 1? *Paleoceanography* **30,** 353–368 (2015).
4. Lund, D. C., Tessin, a C., Hoffman, J. L. & Schmittner, A. Southwest Atlantic water mass evolution during the last deglaciation. *Paleoceanography* **30,** 477–494 (2015).
5. Waelbroeck, C. *et al.* The timing of deglacial circulation changes in the Atlantic. *Paleoceanography* **26,** PA3213 (2011).
6. Skinner, L. C., Shackleton, N. J. & Elderfield, H. Millennial-scale variability of deep-water temperature and δ^{18}Odw indicating deep-water source variations in the Northeast Atlantic, 0-34 cal. ka BP. *Geochem. Geophys. Geosyst.* **4,** 1098 (2003).
7. Skinner, L. C. & Shackleton, N. J. Deconstructing Terminations I and II: revisiting the glacioeustatic paradigm based on deep-water temperature estimates. *Quat. Sci. Rev.* **25,** 3312–3321 (2006).
8. Meland, M. Y., Dokken, T. M., Jansen, E. & Hevrøy, K. Water mass properties and exchange between the Nordic seas and the northern North Atlantic during the period 23-6 ka: Benthic oxygen isotopic evidence. *Paleoceanography* **23,** PA1210 (2008).
9. Thornalley, D. J. R., Elderfield, H. & McCave, I. N. Intermediate and deep water paleoceanography of the northern North Atlantic over the past 21,000 years. *Paleoceanography* **25,** PA1211 (2010).
10. McManus, J. F., Francois, R., Gherardi, J.-M., Keigwin, L. D. & Brown-Leger, S. Collapse and rapid resumption of Atlantic meridional circulation linked to deglacial climate changes. *Nature* **428,** 834–7 (2004).
11. Anderson, R. F. *et al.* Wind-driven upwelling in the Southern Ocean and the deglacial rise in atmospheric CO_2. *Science* **323,** 1443–8 (2009).
12. Shakun, J. D. *et al.* Global warming preceded by increasing carbon dioxide concentrations during the last deglaciation. *Nature* **484,** 49–54 (2012).
13. Roberts, J. *et al.* Evolution of South Atlantic density and chemical stratification across the last deglaciation. *Proc. Natl. Acad. Sci.* **113,** 514–519 (2016).
14. Lea, D. W. in *Treatise on Geochemistry* (Holland, H. D. & Turekian, K. K.) **8,** 373–397 (Elsevier, 2014).
15. Ganopolski, A. & Roche, D. M. On the nature of lead–lag relationships during glacial–interglacial climate transitions. *Quat. Sci. Rev.* **28,** 3361–3378 (2009).
16. Liu, Z. *et al.* Transient simulation of last deglaciation with a new mechanism for Bølling-Allerød warming. *Science* **325,** 310–314 (2009).
17. Smith, R. S. & Gregory, J. The last glacial cycle: transient simulations with an AOGCM.

Clim. Dyn. **38,** 1545–1559 (2012).

18. Friedrich, T. & Timmermann, A. Millennial-scale glacial meltwater pulses and their effect on the spatiotemporal benthic $\delta^{18}O$ variability. *Paleoceanography* **27,** PA3215 (2012).

19. Roche, D. M., Paillard, D., Caley, T. & Waelbroeck, C. LGM hosing approach to Heinrich Event 1: results and perspectives from data–model integration using water isotopes. *Quat. Sci. Rev.* **106,** 247–261 (2014).

20. Bagniewski, W., Meissner, K. J., Menviel, L. & Brennan, C. E. Quantification of factors impacting seawater and calcite $\delta^{18}O$ during Heinrich Stadials 1 and 4. *Paleoceanography* **30,** 895–911 (2015).

21. He, F. Simulating transient climate evolution of the last deglaciation with CCSM3. (2011).

22. Marcott, S. A. *et al.* Ice-shelf collapse from subsurface warming as a trigger for Heinrich events. *Proc. Natl. Acad. Sci. USA* **108,** 13415–9 (2011).

23. Tarutani, T., Clayton, R. N. & Mayeda, T. K. The effect of polymorphism and magnesium substitution on oxygen isotope fractionation between calcium carbonate and water. *Geochim. Cosmochim. Acta* **33,** 987–996 (1969).

24. Shin, S.-I. *et al.* A Simulation of the Last Glacial Maximum climate using the NCAR-CCSM. *Clim. Dyn.* **20,** 127–151 (2003).

25. Curry, W. B. & Oppo, D. W. Glacial water mass geometry and the distribution of $\delta^{13}C$ of ΣCO_2 in the western Atlantic Ocean. *Paleoceanography* **20,** PA1017 (2005).

26. Skinner, L. C., Waelbroeck, C., Scrivner, A. E. & Fallon, S. J. Radiocarbon evidence for alternating northern and southern sources of ventilation of the deep Atlantic carbon pool during the last deglaciation. *Proc. Natl. Acad. Sci. USA* **111,** 5480–4 (2014).

27. Skinner, L. C. & Shackleton, N. J. Rapid transient changes in northeast Atlantic deep water ventilation age across Termination I. *Paleoceanography* **19,** PA2005 (2004).

28. Thiagarajan, N., Subhas, A. V, Southon, J. R., Eiler, J. M. & Adkins, J. F. Abrupt pre-Bølling-Allerød warming and circulation changes in the deep ocean. *Nature* **511,** 75–8 (2014).

29. Palter, J. B. *et al.* The deep ocean buoyancy budget and its temporal variability. *J. Clim.* **27,** 551–573 (2014).

30. Mignot, J., Ganopolski, A. & Levermann, A. Atlantic subsurface temperatures: Response to a shutdown of the overturning circulation and consequences for its recovery. *J. Clim.* **20,** 4884–4898 (2007).

31. Jahn, A. *et al.* Carbon isotopes in the ocean model of the Community Earth System Model (CESM1). *Geosci. Model Dev.* **8,** 2419–2434 (2015).

32. Lambeck, K., Rouby, H., Purcell, A., Sun, Y. & Sambridge, M. Sea level and global ice volumes from the Last Glacial Maximum to the Holocene. *Proc. Natl. Acad. Sci.* **111,** 15296–15303 (2014).

33. Danabasoglu, G. *et al.* The CCSM4 Ocean Component. *J. Clim.* **25,** 1361–1389 (2012).

34. Hurrell, J. W. *et al.* The Community Earth System Model: A framework for collaborative research. *Bull. Am. Meteorol. Soc.* **94,** 1339–1360 (2013).

35. Schmidt, G. A. Forward modeling of carbonate proxy data from planktonic foraminifera using oxygen isotope tracers in a global ocean model. *Paleoceanography* **14,** 482–497 (1999).

36. Orr, J., Najjar, R., Sabine, C. & Joos, F. *Abiotic-HOWTO*. (1999).

37. Fiadeiro, M. E. Three-dimensional modeling of tracers in the deep Pacific Ocean II: radiocarbon and the circulation. *J. Mar. Res.* **40,** 537–550 (1982).

38. Tziperman, E., Toggweiler, J. R., Bryan, K. & Feliks, Y. Instability of the thermohaline circulation with respect to mixed boundary conditions: Is it really a problem for realistic models? *J. Phys. Oceanogr.* **24,** 217–232 (1994).

39. Liu, Z. *et al.* Chinese cave records and the East Asia Summer Monsoon. *Quat. Sci. Rev.* **83,** 115–128 (2014).

40. Sima, A., Paul, A., Schulz, M. & Oerlemans, J. Modeling the oxygen-isotopic composition of the North American Ice Sheet and its effect on the isotopic composition of the ocean during the last glacial cycle. *Geophys. Res. Lett.* **33,** L15706 (2006).

41. Stenni, B. *et al.* Expression of the bipolar see-saw in Antarctic climate records during the last deglaciation. *Nat. Geosci.* **4,** 46–49 (2011).

42. Steig, E. J. *et al.* Change in climate, ocean and ice-sheet conditions in the Ross embayment, Antarctica, at 6 ka. *Ann. Glaciol.* **27,** 305–310 (1998).

43. Joos, F. & Spahni, R. Rates of change in natural and anthropogenic radiative forcing over the past 20,000 years. *Proc. Natl. Acad. Sci.* **105,** 1425–1430 (2008).

44. Reimer, P. J. *et al.* INTCAL09 and MARINE09 radiocabon age calibration curves, 0-50,000 years cal BP. *Radiocarbon* **51,** 1111–1150 (2009).

45. Shackleton, N. J. Attainment of isotopic equilibrium between ocean water and the benthonic foraminifera genus Uvigerina: Isotopic changes in the ocean during the last glacial. *Colloq. Int. C.N.R.S.* **219,** 203–209 (1974).

46. Hut, G. *Consultants' group meeting on stable isotope reference samples for geochemical and hydrological investigations*. (1987).

47. Stern, J. V. & Lisiecki, L. E. Termination 1 timing in radiocarbon-dated regional benthic $\delta^{18}O$ stacks. *Paleoceanography* **29,** 1127–1142 (2014).

48. Griffies, S. M. *et al. Datasets and protocol for the CLIVAR WGOMD Coordinated Ocean-sea ice Reference Experiments (COREs)*. (2012).

49. Deschamps, P. *et al.* Ice-sheet collapse and sea-level rise at the Bølling warming 14,600 years ago. *Nature* **483,** 559–64 (2012).

50. Clark, P. U., Mitrovica, J. X., Milne, G. A. & Tamisiea, M. E. Sea-level fingerprinting as a direct test for the source of global meltwater pulse IA. *Science* **295,** 2438–2441 (2002).

51. Weaver, A. J., Saenko, O. a, Clark, P. U. & Mitrovica, J. X. Meltwater pulse 1A from Antarctica as a trigger of the Bølling-Allerød warm interval. *Science* **299,** 1709–13 (2003).

52. Clark, P. U. *et al.* Origin of the first global meltwater pulse following the Last Glacial Maximum. *Paleoceanography* **11,** 563 (1996).

53. Vidal, L. *et al.* Evidence for changes in the North Atlantic Deep Water linked to meltwater surges during the Heinrich events. *Earth Planet. Sci. Lett.* **146,** 13–27 (1997).

54. Waelbroeck, C. *et al.* The timing of the last deglaciation in North Atlantic climate records. *Nature* **412,** 724–7 (2001).

55. Labeyrie, L., Waelbroeck, C., Cortijo, E., Michel, E. & Duplessy, J.-C. Changes in deep water hydrology during the Last Deglaciation. *Comptes Rendus Geosci.* **337,** 919–927 (2005).

56. Gherardi, J. -M. *et al.* Glacial-interglacial circulation changes inferred from 231Pa/230Th sedimentary record in the North Atlantic region. *Paleoceanography* **24,** PA2204 (2009).

57. Griffies, S. M. The Gent–McWilliams skew flux. *J. Phys. Oceanogr.* **28,** 831–841 (1998).

58. Skinner, L. C. & Shackleton, N. J. An Atlantic lead over Pacific deep-water change across Termination I: implications for the application of the marine isotope stage stratigraphy. *Quat. Sci. Rev.* **24,** 571–580 (2005).

59. Lisiecki, L. E. & Raymo, M. E. Diachronous benthic $\delta^{18}O$ responses during late Pleistocene terminations. *Paleoceanography* **24,** PA3210 (2009).

60. Dokken, T. M. & Jansen, E. Rapid changes in the mechanism of ocean convection during the last glacial period. *Nature* **401,** 458–461 (1999).

61. Rasmussen, T. L., Thomsen, E., Labeyrie, L. & van Weering, T. C. E. Circulation changes in the Faroe-Shetland Channel correlating with cold events during the last glacial period (58-10ka). *Geology* **24,** 937–940 (1996).

62. Rasmussen, T. L., Thomsen, E. & van Weering, T. C. E. Cyclic sedimentation on the Faeroe Drift 53-10 ka BP related to climatic variations. in *Geol. Process. on Continental Margins Sedimentation, Mass-Wasting and Stability* (Stoker, M. S., Evans, D. & Cramp, A.) **129,** 255–267 (Geological Society Special Publications, 1998).

63. Rasmussen, T. L., Oppo, D. W., Thomsen, E. & Lehman, S. J. Deep sea records from the southeast Labrador Sea: Ocean circulation changes and ice-rafting events during the last 160,000 years. *Paleoceanography* **18,** 1018 (2003).

64. Voelker, A. H. L. *et al.* Mediterranean outflow strengthening during northern hemisphere coolings: A salt source for the glacial Atlantic? *Earth Planet. Sci. Lett.* **245,** 39–55 (2006).

65. Tjallingii, R. *et al.* Coherent high- and low-latitude control of the northwest African hydrological balance. *Nat. Geosci.* **1,** 670–675 (2008).

66. Collins, J. A. *et al.* Interhemispheric symmetry of the tropical African rainbelt over the past 23,000 years. *Nat. Geosci.* **4,** 42–45 (2011).

67. Sarnthein, M. *et al.* Changes in East Atlantic Deepwater Circulation over the last 30,000 years: Eight time slice reconstructions. *Paleoceanography* **9,** 209–267 (1994).

68. Mulitza, S. *et al.* Sahel megadroughts triggered by glacial slowdowns of Atlantic meridional overturning. *Paleoceanography* **23,** PA4206 (2008).

69. Rühlemann, C., Mulitza, S., Müller, P. J., Wefer, G. & Zahn, R. Warming of the tropical Atlantic Ocean and slowdown of thermohaline circulation during the last deglaciation. *Nature* **402,** 511–514 (1999).

70. Rühlemann, C. *et al.* Intermediate depth warming in the tropical Atlantic related to weakened thermohaline circulation: Combining paleoclimate data and modeling results for the last deglaciation. *Paleoceanography* **19,** PA1025 (2004).

71. Zahn, R. & Stüber, A. Suborbital intermediate water variability inferred from paired benthic foraminiferal Cd/Ca and $\delta^{13}C$ in the tropical West Atlantic and linking with North Atlantic climates. *Earth Planet. Sci. Lett.* **200,** 191–205 (2002).

72. Curry, W. B. & Oppo, D. W. Synchronous, high-frequency oscillations in tropical sea surface temperatures and North Atlantic Deep Water production during the last glacial cycle. *Paleoceanography* **12,** 1–14 (1997).

73. Ostermann, D. R. & Curry, W. B. Calibration of stable isotopic data: An enriched $\delta^{18}O$ standard used for source gas mixing detection and correction. *Paleoceanography* **15,** 353–360 (2000).

74. Little, M. G. *et al.* Rapid palaeoceanographic changes in the Benguela Upwelling System for the last 160,000 years as indicated by abundances of planktonic foraminifera. *Palaeogeogr. Palaeoclimatol. Palaeoecol.* **130,** 135–161 (1997).

75. Vidal, L. *et al.* Link between the North and South Atlantic during the Heinrich events of the last glacial period. *Clim. Dyn.* **15,** 909–919 (1999).

76. Sortor, R. N. & Lund, D. C. No evidence for a deglacial intermediate water $\Delta^{14}C$ anomaly in the SW Atlantic. *Earth Planet. Sci. Lett.* **310,** 65–72 (2011).

77. Tessin, a. C. & Lund, D. C. Isotopically depleted carbon in the mid-depth South Atlantic during the last deglaciation. *Paleoceanography* **28,** 296–306 (2013).

78. Hoffman, J. L. & Lund, D. C. Refining the stable isotope budget for Antarctic Bottom Water: New foraminiferal data from the abyssal southwest Atlantic. *Paleoceanography* **27,** PA1213 (2012).

79. Dickson, A. J. *et al.* Oceanic forcing of the Marine Isotope Stage 11 interglacial. *Nat. Geosci.* **2,** 428–433 (2009).